

# Optical mode structure of the air waveguide

N. Jhaji, J. K. Wahlstrand, and H. M. Milchberg\*

*Institute for Research in Electronics and Applied Physics, University of Maryland, College Park, Maryland 20742, USA*

\*Corresponding author: milch@umd.edu

Received September 2, 2014; revised September 30, 2014; accepted October 3, 2014;  
posted October 6, 2014 (Doc. ID 222307); published October 29, 2014

Analysis is performed on propagation of light in long-lived optical waveguides in air generated by arrays of femto-second filaments. Mode structure, leakage losses, and coupling efficiency are studied analytically and numerically as a function of wavelength and time delay after the waveguide-initiating filaments. © 2014 Optical Society of America

OCIS codes: (010.1300) Atmospheric propagation; (230.7370) Waveguides.  
<http://dx.doi.org/10.1364/OL.39.006312>

When intense ultrashort optical pulses propagate through the atmosphere, the dynamic interplay between Kerr self-focusing and plasma defocusing can result in propagation of a core of high optical intensity over distances much greater than a Rayleigh length corresponding to the core diameter [1,2]. We have recently shown that the energy nonlinearly deposited in the air by the filament core, from plasma generation and molecular excitation, induces a long timescale hydrodynamic response [3–5]. This response makes possible the creation of long-lived optical waveguiding structures having potential for both guiding high power laser beams [6] and for remote collection of weak optical signals [7]. Potential applications for both transmission and collection include directed energy [8], lightning control [9], atmospheric lasing [10,11], LIDAR [12], laser-induced breakdown spectroscopy (LIBS) [13], and versions of resonance-enhanced multiphoton ionization (REMPI) spectroscopy [14]. Essential to the practical use of air waveguides is an analysis of their optical properties. In this Letter, we explore the modal and light transport properties of air waveguide structures using analytical and numerical methods.

The optical properties of air waveguides depend on the evolving air density profile, which is determined by the axial and transverse distribution of energy deposited in the gas by the filament or filament array. In a single femtosecond filament in air at standard conditions, energy is absorbed through ionization and two-photon excitation of rotational states. For typical pulse durations of ~40–100 fs, approximately 25 mJ/cm<sup>3</sup> is deposited over the ~50 μm radius filament core [3,5,15] by plasma generation and molecular rotational excitation. The hydrodynamic response of air to this pressure impulse leads, over a ~100 ns timescale, to the formation of an outgoing, single-cycle cylindrical acoustic wave, which leaves behind a region of hot gas and a corresponding density depression [3]. The density depression or ‘hole’ then decays by thermal diffusion over milliseconds. The refractive index profile enabling air waveguiding is related to the change in density by  $\Delta n/(n_0 - 1) = \Delta\rho/\rho_0$ , where  $\Delta n$  is the change in refractive index,  $n_0 - 1 = 2.8 \times 10^{-4}$  is the index of refraction of air at ambient density  $\rho_0$ , and  $\Delta\rho$  is the change in density. The hydrodynamic response of the gas is simulated using a 1D Lagrangian hydrocode where we take the initial energy deposition to be 25 mJ/cm<sup>3</sup>. Details of the code can be found in earlier work [3,5,6].

We consider the two regimes of guiding demonstrated in our prior work, *acoustic* and *thermal* guiding. Acoustic guiding, which typically occurs over a microsecond time-scale interval [5–7], works by confining light in the positive density (refractive index) crest of the single cycle annular acoustic wave launched from a single filament [5,16], or in the enhanced density peak resulting from collision of acoustic waves from multiple filaments [5,6] (see Fig. 1). In the much longer lived, millisecond scale thermal guiding regime [3,6,7], a ring of  $\geq 4$  filaments leaves a cladding ‘moat’ of diffusively merged density holes surrounding a near ambient air density core (see Fig. 2).

In order to discuss mode structure, we consider idealized air waveguides whose transverse refractive index profile is axially invariant. While real air waveguides have axial variation [5–7] the scale is over many Rayleigh ranges of the guided beam. We also neglect any absorption or scattering losses, which can be added with an exponential attenuation factor. To find the modes  $A(\mathbf{r}_\perp, z)e^{i\beta z}$ , where  $A$  is a slowly varying field amplitude and  $\mathbf{r}_\perp$  and  $z$  are transverse and axial coordinates, we consider the paraxial scalar wave equation

$$2i\beta \frac{\partial A(\mathbf{r}_\perp, z)}{\partial z} + [\nabla_\perp^2 + (k^2 n^2(\mathbf{r}_\perp) - \beta^2)]A(\mathbf{r}_\perp, z) = 0, \quad (1)$$

where  $k$  is the vacuum wavenumber,  $n(\mathbf{r}_\perp) = n_0 + \Delta n(\mathbf{r}_\perp)$  is the air refractive index (assumed dispersionless for our range of considered wavelengths),  $\Delta n(\mathbf{r}_\perp)$  is the filament-induced refractive index profile change, and  $\beta$  is the waveguide wavenumber. Use of the scalar wave equation is well justified, as the air waveguides created in the wake of filamentation are all well within the weak guiding regime [17,18]; index shifts are of order  $|\Delta n|/n_0 \approx 10^{-5}$ . For later use in our analysis, we define an effective mode index  $\tilde{n}$  by  $\beta = k(n_0 + \tilde{n})$ .

The type of mode supported depends on the profile details of the guide. Profiles with a region or regions of positive refractive index with respect to the surrounding air can support strictly bound modes [17], which propagate with no transverse leakage loss. This applies to both the single and multifilament acoustic guides, where there are regions of increased air density with respect to the ambient density. In contrast, thermal guides support only leaky modes [17] because the index perturbation from the density holes is strictly negative. Leaky modes have an oscillatory component at large  $|\mathbf{r}_\perp|$  that corresponds

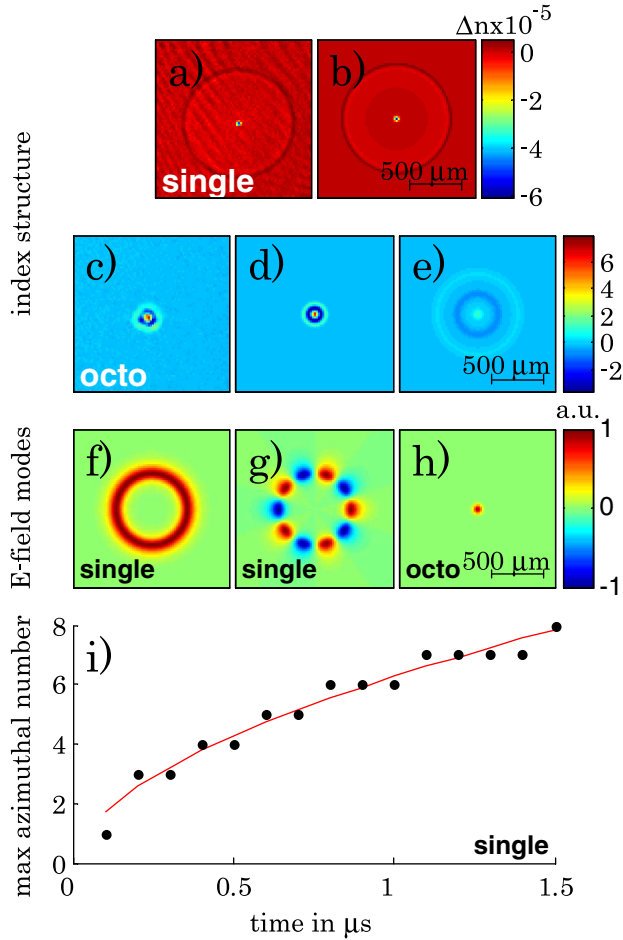


Fig. 1. Mode properties at  $\lambda = 532$  nm of single and octo-filament induced acoustic guides. Measured air refractive index profiles for single (a) and octo-filament excitation (c), along with corresponding hydrocode-simulations (b),(d). Panel (e) shows an index profile simulation for the larger transverse scale typical of axially extended air waveguides. Calculated modes for the single filament-induced acoustic annular guide are shown in (f)  $p = 0, m = 0$  and (g)  $p = 0, m = 5$ . The lowest order mode for the guide of (e) is shown in (h). Panel (i) shows the maximum azimuthal mode number  $m_{\max}$  versus delay for the single filament-induced annular guide. Points: simulation, red curve: best fit.

to the leakage of energy out of the guide as the light propagates [18]. However, we will show that the propagation losses per unit length for these guides can be quite small.

To find the bound modes of air waveguides that can support them, we set  $\partial/\partial z = 0$  in Eq. (1), leaving the transverse Helmholtz equation which we solve numerically. For azimuthally symmetric guides, the solutions are indexed by radial ( $p$ ) and azimuthal ( $m$ ) mode numbers. To find the fundamental leaky mode of an arbitrary leaky structure, we apply the beam propagation method (BPM) [19] to Eq. (1) (for  $\partial/\partial z \neq 0$ ) using a suitable initial guess  $A(\mathbf{r}_\perp, 0)$  and sufficient propagation distance that  $|\partial A/\partial z|$  is small and the solution, apart from a weak exponential decay along  $z$ , approaches a steady state transverse shape. This method is equivalent to shedding any higher order leaky modes.

Figures 1(a) and 1(b) show experimental and simulated index profiles for the single filament-induced

acoustic guide at time  $t = 500$   $\mu\text{s}$  after the filament. The amplitude and radial scale (or wavelength) of the outgoing density perturbation is imposed by the strength and diameter  $a$  of the initiating filament energy deposition. Figures 1(f) and 1(g) show calculated bound modes at  $\lambda = 532$  nm for  $(p, m) = (0, 0)$  and  $(0, 5)$ , confirming that the mode conforms to the acoustic wave peak [5,16]. At typical levels of energy deposition in filaments, the density modulation is not deep or wide enough to support higher order ( $p > 0$ ) radial modes. As the acoustic wave expands outward, higher order azimuthal modes with  $\cos m\phi$  dependence are allowed, with the highest azimuthal mode number scaling as  $m_{\max} \sim R^{0.6}$ , as seen in Fig. 1(i), where  $R = c_s t$  is the ring radius,  $c_s$  is the acoustic speed and  $t$  is time after the filament energy deposition. Prior experiments and simulations of trapping in single filament acoustic guides have shown a useful window of  $\sim 1$   $\mu\text{s}$  over which optimally positioned Gaussian beams can be efficiently coupled [5,16].

In the multifilament acoustic guide, each of the filaments, equidistant from a common center, launches a single cycle acoustic wave. The interference maximum produced when the waves meet on axis typically lasts  $\tau \sim a/c_s < \sim 1$   $\mu\text{s}$ , a timescale scale set by the sound speed and acoustic wavelength (here  $\sim 300$  ns). Figures 1(c) and 1(d) show an interferometric measurement of an octo-filament-induced acoustic guide at the moment of peak central index enhancement at delay  $\sim 200$  ns and its hydrocode simulation using a ring-shaped pressure source [5]. Guides as in Fig. 1(c), amenable to longitudinal interferometry, are shorter with tighter transverse spatial features [5,6]. A hydrocode simulation more representative of our axially extended structures used for guiding [6,7] is shown in Fig. 1(e) for an initial ring pressure source of radius  $200$   $\mu\text{m}$  with the same total energy deposition as for 8 filaments. The  $p = 0, m = 0$  mode for this guide is shown in Fig 1(h), peaking on axis, in contrast to the fundamental ring-shaped mode of the single filament-induced acoustic guide [Fig. 1(c)]. For typical parameters, such multifilament acoustic guides only support the lowest order mode.

As discussed earlier, for thermal guides generated by a ring array of filaments, leaky guiding occurs, with the field energy contained in the ambient density core bounded by the lower density moat where the filaments were located. Row (a) of Fig. 2 shows interferometric measurements of short octo-filament arrays for several times during the evolution of the thermal guide. The three panels resolve distinct stages of the evolution: At  $t = 2$   $\mu\text{s}$  the density holes from individual filaments are still distinct, at  $t = 10$   $\mu\text{s}$  the holes have merged through thermal diffusion to form a continuous ring, and at  $t = 50$   $\mu\text{s}$  the holes have diffused to the center and have washed-out the guide. Figures 2(b) and 2(c) show larger transverse scale simulations consistent with longer multi-filaments used in guiding experiments [6,7]. As can be seen, the relevant timescales increase with the transverse scale size, with guide washout now occurring at  $> 1.5$  ms. In Fig. 2(b) the linearity of gas hydrodynamics for small density perturbations allows the summation of single filament results from our 1D hydrocode [5] to obtain an excellent approximation to the 2D response to the octo-filament. Figure 2(c) shows the efficacy of treating the

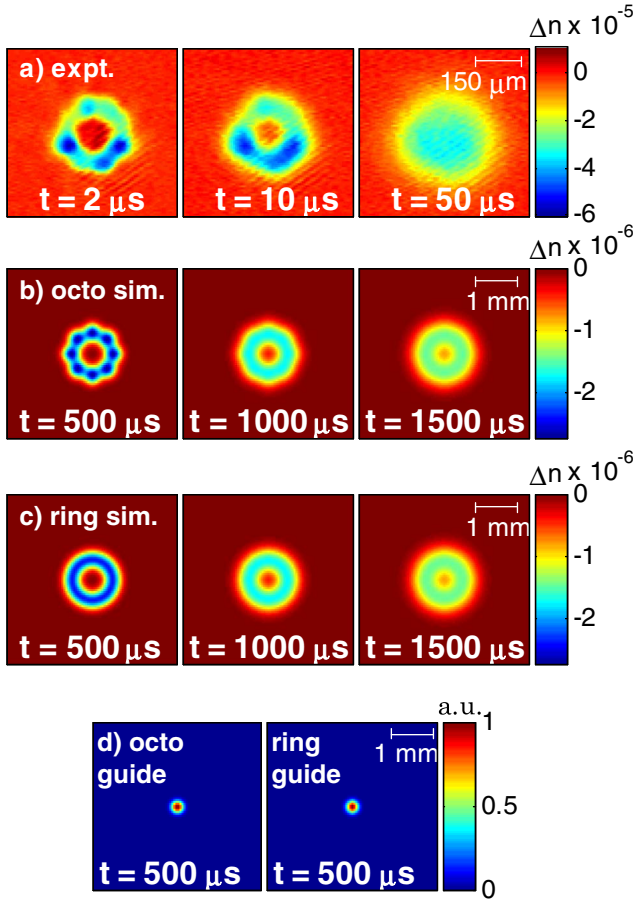


Fig. 2. Typical refractive index profiles and modes of thermal air waveguides. (a) Interferometrically measured refractive index profiles, (b) simulated time evolution of eight-lobe filament with 500  $\mu\text{m}$  ring radius, (c) simulated time evolution of ring heat source with 500  $\mu\text{m}$  ring radius and initial energy deposition equal to the eight-lobe filament case, (d) calculated fundamental leaky modes at  $\lambda = 532$  nm of the octo-lobe and ring air waveguides shown in (b) and (c).

octo-filament array as a continuous ring heat source with the same total initial energy. In contrast with the acoustic regime, the thermal regime produces a much longer lasting guide whose lifetime  $\tau_{\text{thermal}} \approx R^2/4\alpha \sim 1$  ms [3], is set by the thermal diffusivity of the gas ( $\alpha = 19 \mu\text{m}^2/\mu\text{s}$  for air at standard conditions [20]) and the transverse length scale of the guide (here  $R = 500 \mu\text{m}$ ).

The fundamental leaky modes for the eight-lobe and idealized ring thermal guides, shown in Fig. 2(d), are close to Gaussian in shape and nearly identical. Even at the early time  $t = 500 \mu\text{s}$ , where there is a marked difference between the eight-lobed and ring index structures [Figs. 2(b) and 2(c)], the overlap integral between the two modes is  $>0.995$ .

We find that the propagation leakage loss from the ring guide of Fig. 2(c) closely approximates that for the octo-thermal guide of Fig. 2(b). Computed loss rates shown in Fig. 3(a) for the ring guide (in red) and the octo-guide (in blue) are nearly identical except at early times, when the gaps between the octo-lobes cause higher loss. Approximate expressions for the axial loss rate  $\gamma = \text{Im}(\beta)$  and effective index  $\tilde{n}$  of the lowest order mode can be derived

assuming a step index decrement  $\Delta n (> 0)$  at the moat of width  $\Delta r$ ,

$$\gamma = \frac{\kappa_{\text{co}}\kappa_{\text{cl}}}{k} \frac{e^{-2\kappa_{\text{cl}}\Delta r}}{\kappa_{\text{cl}}r_{\text{co}} + 1 - e^{-2\kappa_{\text{cl}}\Delta r}}, \quad (2a)$$

$$\tilde{n} \approx \Delta n - \frac{1}{2k^2r_{\text{co}}^2} [1 + \ln(2\Delta nk^2r_{\text{co}}^2)], \quad (2b)$$

where  $r_{\text{co}}$  is the core radius, and  $\kappa_{\text{co}} = k[2(\Delta n - \tilde{n})]^{1/2}$  and  $\kappa_{\text{cl}} = k(2\tilde{n})^{1/2}$  are propagation constants in the core and cladding. Since the lowest order leaky mode is nearly Gaussian [Fig. 2(d)] we used a variational equation with Gaussian trial function to derive Eq. (2b). At early times up to  $\sim 500 \mu\text{s}$ , propagation loss decreases as there is less transverse leakage through a broad and shallow cladding region than through a narrow and deep one. Beyond  $\sim 500 \mu\text{s}$  the trend reverses as the density hole diffusion reduces the central density, decreasing the index contrast between the core and cladding. Loss rates versus delay for a range of wavelengths are plotted in Fig. 3(b), where the wavelength dependence at fixed delay stems from the increase in guided mode size with wavelength, which is accompanied by larger leakage losses.

Figure 4 shows coupling efficiency at  $\lambda = 532$  nm into various guides for a varying Gaussian beam waist diameter, with the waist located at the waveguide entrance and centered on the guide axis. Coupling efficiency is defined as the overlap integral between the Gaussian beam and the modes of the guide. For the single filament acoustic guide, coupling only occurs into the lowest order mode, as azimuthal symmetry of the Gaussian beam prevents coupling into any higher order modes. Highest coupling efficiency is achieved at early times, but the presence of the deep density hole on axis requires the coupled mode to be large. At longer times, the optimal waist size increases linearly in time, following the acoustic wave location  $r = c_s t$ . However, coupling efficiency falls as  $t^{-1}$  because the beam area increases as  $r^2$  to overlap an acoustic ring area increasing as  $r$ . Maximum coupling efficiency to the multifilament acoustic guide occurs when the inward propagating acoustic waves collide on axis, which occurs just beyond 1  $\mu\text{s}$  in Fig. 4(b). For a waist of 70  $\mu\text{m}$ , the coupling efficiency is  $>85\%$  over a duration of  $\sim 250$  ns. For the octo-filament-induced thermal guide [Fig. 4(c)], the lowest order mode is nearly Gaussian; we find that

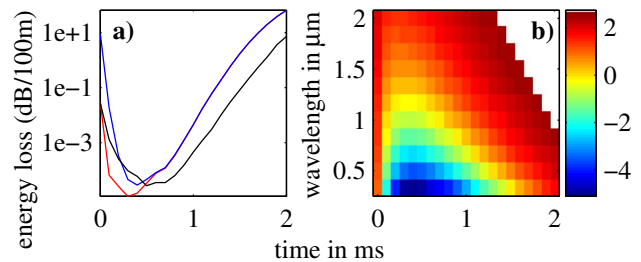


Fig. 3. (a) Energy loss at  $\lambda = 532$  nm in dB/100 m for the octo-lobe index and ring index structures of Fig. 2 (blue and red respectively) and from the expression for  $\gamma$  in Eq. (2) (black). (b) Loss in dB/100 m versus time for a range of wavelengths (color scale in log base 10).

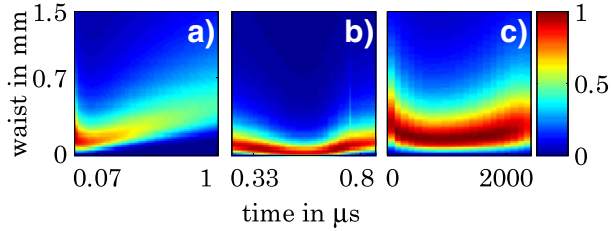


Fig. 4. Coupling efficiency of a Gaussian beam at focus as a function of time and waist size for the (a) single filament acoustic guide, (b) octo-filament acoustic guide, and (c) octo-filament thermal guide.

optimal coupling efficiency is  $>95\%$  for approximately the first millisecond. As one can see, there is a very broad range of nearly optimal waist sizes with a full width at half maximum spanning  $\sim 400\ \mu\text{m}$ .

In conclusion, we have found and characterized optical modes of the distinct types of air waveguides that are formed in the wake of femtosecond filaments or filament arrays. The acoustic wave from a single filament supports only ring-shaped optical modes, with an increasing number of azimuthal modes with time. However, the coupling efficiency for an injected Gaussian beam falls as  $t^{-1}$ , fading away by  $\sim 1\ \mu\text{s}$ . The multifilament acoustic guide primarily supports lowest order modes peaked on axis, but likewise has an efficient coupling lifetime of  $\sim 1\ \mu\text{s}$ . The thermal air waveguides studied here support near-Gaussian low loss leaky modes. We examined their leakage loss as a function of delay, wavelength, and guide characteristics. Gaussian beam coupling of  $>95\%$  efficiency is possible over the millisecond scale lifetime of the guide.

This research is supported by the Air Force Office of Scientific Research, the Defense Threat Reduction Agency, the Army Research Office, and the National Science Foundation.

## References

1. A. Couairon and A. Mysyrowicz, *Phys. Rep.* **441**, 47 (2007).
2. L. Bergé, S. Skupin, R. Nuter, J. Kasparian, and J.-P. Wolf, *Rep. Prog. Phys.* **70**, 1633 (2007).
3. Y.-H. Cheng, J. K. Wahlstrand, N. Jhajj, and H. M. Milchberg, *Opt. Express* **21**, 4740 (2013).
4. N. Jhajj, Y.-H. Cheng, J. K. Wahlstrand, and H. M. Milchberg, *Opt. Express* **21**, 28980 (2013).
5. J. K. Wahlstrand, N. Jhajj, E. W. Rosenthal, S. Zahedpour, and H. M. Milchberg, *Opt. Lett.* **39**, 1290 (2014).
6. N. Jhajj, E. W. Rosenthal, R. Birnbaum, J. K. Wahlstrand, and H. M. Milchberg, *Phys. Rev. X* **4**, 011027 (2014).
7. E. W. Rosenthal, N. Jhajj, J. K. Wahlstrand, and H. M. Milchberg, *Optica* **1**, 5 (2014).
8. P. Sprangle, J. Peñano, and B. Hafizi, *J. Direct Energy* **2**, 71 (2006).
9. J.-C. Diels, R. Bernstein, K. E. Stahlkopf, and X. M. Zhao, *Sci. Am.* **277**, 50 (1997).
10. A. Dogariu, J. B. Michael, M. O. Scully, and R. B. Miles, *Science* **331**, 442 (2011).
11. P. Sprangle, J. Peñano, B. Hafizi, D. Gordon, and M. Scully, *Appl. Phys. Lett.* **98**, 211102 (2011).
12. J. Kasparian, M. Rodriguez, G. Méjean, J. Yu, E. Salmon, H. Wille, R. Bourayou, S. Frey, Y.-B. André, A. Mysyrowicz, R. Sauerbrey, J.-P. Wolf, and L. Wöste, *Science* **301**, 61 (2003).
13. P. Rohwetter, J. Yu, G. Mejean, K. Stelmasczyk, E. Salmon, J. Kasparian, J.-P. Wolf, and L. Wöste, *J. Anal. At. Spectrom.* **19**, 437 (2004).
14. A. Dogariu and R. B. Miles, *Appl. Opt.* **50**, A68 (2011).
15. S. Zahedpour, J. K. Wahlstrand, and H. M. Milchberg, *Phys. Rev. Lett.* **112**, 143601 (2014).
16. L. Levi, O. Lahav, R. A. Nemirovsky, J. Nemirovsky, I. Orr, I. Kaminer, M. Segev, and O. Cohen, *Phys. Rev. A* **90**, 021801 (2014).
17. A. W. Snyder and J. D. Love, *Optical Waveguide Theory* (Chapman & Hall, 1983).
18. T. R. Clark and H. M. Milchberg, *Phys. Rev. E* **61**, 1954 (2000).
19. M. D. Feit and J. Fleck, *Appl. Opt.* **17**, 3990 (1978).
20. W. M. Haynes, *Handbook of Chemistry and Physics*, 93rd ed. (CRC Press, 2012), <http://www.hbcpnetbase.com/>.